Hierarchical Nano/Micro-Structured Surfaces With High Surface Area/Volume Ratios

Ketki M. Lichade
Department of Mechanical and Industrial Engineering,
University of Illinois at Chicago,
Chicago, IL 60607
e-mail: klicha2@uic.edu

Yizhou Jiang
Department of Mechanical and Industrial Engineering,
University of Illinois at Chicago,
Chicago, IL 60607
e-mail: yjiang89@uic.edu

Yayue Pan[1]
Department of Mechanical and Industrial Engineering,
University of Illinois at Chicago,
Chicago, IL 60607
e-mail: yayuepan@uic.edu

Recently, many studies have investigated additive manufacturing (AM) of hierarchical surfaces with high surface area/volume (SA/V) ratios, and their performance has been characterized for applications in next-generation functional devices. Despite recent advances, it remains challenging to design and manufacture high SA/V ratio structures with desired functionalities. In this study, we established the complex correlations among the SA/V ratio, surface structure geometry, functionality, and manufacturability in the two-photon polymerization (TPP) process. Inspired by numerous natural structures, we proposed a 3-level hierarchical structure design along with the mathematical modeling of the SA/V ratio. Geometric and manufacturing constraints were modeled to create well-defined three-dimensional hierarchically structured surfaces with a high accuracy. A process flowchart was developed to design the proposed surface structures to achieve the target functionality, SA/V ratio, and geometric accuracy. Surfaces with varied SA/V ratios and hierarchy levels were designed and printed. The wettability and antireflection properties of the fabricated surfaces were characterized. It was observed that the wetting and antireflection properties of the 3-level design could be easily tailored by adjusting the design parameter settings and hierarchy levels. Furthermore, the proposed surface structure could change a naturally hydrophilic surface to near-superhydrophobic. Geometrical light trapping effects were enabled and the antireflection property could be significantly enhanced (> 80% less reflection) by the proposed hierarchical surface structures. Experimental results implied the great potential of the proposed surface structures for various applications such as microfluidics, optics, energy, and interfaces.
[DOI: 10.1115/1.4049850]

Keywords: bio-inspired structure, hierarchical structure, two-photon polymerization, superhydrophobic surfaces, antireflection, additive manufacturing

1 Introduction

Artificial nano/microstructures with high surface area/volume (SA/V) ratios have received extensive attention due to their potential in a wide range of applications such as flexible electronics [1,2], microfluidics [3], and tissue engineering [4]. For instance, in the energy storage field, high SA/V geometries enable rapid ionic transportation and ultrahigh power density [5]. Innovative surfaces with high SA/V geometries can also improve the hydrophobicity, which is beneficial to the fabrication of complicated microfluidic devices [6]. In addition, scaffolds with a high SA/V ratio are significant to cell-based studies in bioengineering applications [7,8].

One of the most common approaches that have been used to increase the SA/V ratio is building hierarchical structures. Many interesting and novel hierarchical structures from living beings have been observed. It has been reported that the surface of some biological systems, such as lotus leaves [9–12], are generally highly hierarchical, resulting in a large SA/V. These hierarchical surface structures enable advanced functionalities such as superhydrophobicity and antireflection. For example, the highly hierarchical cone-shaped crystals on the lotus leaf surface can increase the hydrophobicity, resulting in anti-adhesion protection [13]. Similarly, the hexagonally close-packed cone-shaped structures observed in cicada wings exhibit anti-bacterial property [14]. Furthermore, in some specific structures, surface wrinkles have been integrated into these existing hierarchical structures to further enhance the SA/V ratio. For instance, surface wrinkles found on the cone-shaped surface structures observed in Rudbeckia, Biden, Viola, Dahlia, and Rosa are beneficial to hydrophobicity [15] and antireflection [16]. Guo et al. performed extensive research to investigate biomimetic surfaces and their applications. They have proposed 15 different combinations of designs, which can be considered as 2-level hierarchical, including cone and wrinkle structures [17]. Most of these natural hierarchical structures show nanoscale and/or micro-scale patterned cone structures integrated with cuticles and winkles, substantially increasing the SA/V ratio of the surface and significantly improving or even enabling functionalities. Reported work in these and many other Refs. [18–20] demonstrated that building hierarchical surface structures with high SA/V ratios is a promising method to enhance functionalities.

To fabricate such hierarchical surface structures, several chemical and physical approaches have been investigated, including chemical etching [21], immersing [22], laser machining [23], and imprinting [24]. Yao et al. fabricated a novel water-repellent surface by a chemical-based deposition method, which involves the copper hydroxide nano-needle array coating on the copper surface [25]. Shang et al. developed a superhydrophobic hierarchical sponge for oil/water separation by immersing approach [26]. Chen et al. successfully fabricated a series of wetting surfaces consisting of conical microstructures at different aspect ratios (ARs) via laser microfabrication [27]. Moreover, inspired by the moth eye's structure, Kuo et al. fabricated antireflective surfaces based on the nano-imprinting lithography technique [28]. Although these techniques have successfully produced hierarchically structured surfaces, the processes usually involve multiple steps and platforms, requiring expensive tools for multi-scale hierarchical manufacturing, and are time-consuming for customization or small-volume production. In addition, most methods can only create two-and-a-half-dimensional (2.5D), rather than three-dimensional (3D) structures.

[1]Corresponding author.
Manuscript received August 26, 2020; final manuscript received January 6, 2021; published online March 26, 2021. Assoc. Editor: Ran Jin.

Recent advances in additive manufacturing (AM) enable the fabrication of more complex designs with ultrahigh resolutions and relatively easy operations [29–36]. Two-photon polymerization (TPP), as one of the most advanced AM techniques, has become a promising approach to directly construct complex three-dimensional (3D) parts in the sub-micron scale or even nanoscale [37,38]. During the TPP process, based on the digital file, the corresponding voxel in the photosensitive liquid gets polymerized once two photons are simultaneously absorbed at the center of the tightly focused laser beam. The part is built in a voxel-by-voxel manner. Moreover, the printing resolution of the TPP process can be as high as 40 nm [39]. The ultrahigh resolution enables numerous applications, including 3D hierarchical structure fabrication with a high degree of spatial controllability [40,41]. For instance, Zyla et al. used the TPP method and successfully fabricated a hierarchical lamellar microstructure inspired by Morpho butterfly [42]. Thangaraju and Dhanapal fabricated hierarchical pyramid structures to create superhydrophobic surfaces using the TPP process [7]. Moreover, Ha et al. developed highly hierarchical 3D meshed microstructures using the TPP process [43]. Despite the advances of the TPP process and all these efforts to create hierarchical structures, very few studies investigated the influence of the hierarchical design parameters on the resulted SA/V ratio and surface functionalities. Therefore, there is an urgent need to establish the link between the design parameters, the SA/V ratio, and surface functionality to understand the structural impact on the functionalities.

Another knowledge gap exists in the design and the TPP manufacturing process planning for high SA/V surface fabrications at the sub-micron scale. Understanding the key manufacturing constraints is crucial to ensure the manufacturability of the design. Typical constraints in the TPP process include (1) the smallest printable feature size, (2) *XY* resolution, and (3) *Z* resolution. As reported by Lee et al., the fabricated pattern in the TPP process can be slightly larger than the designed CAD model with undesirable geometric errors [44]. Such geometric errors originate from the arrangement of voxels on the contour of the printed geometry, causing significant defects in surface finish. High surface finish and geometric accuracy are crucial in many engineering applications. A common approach is to compensate the geometric error in the original CAD model design [45]. To implement this method, the manufacturing constraints need to be understood, and relations between design parameters and geometric errors need to be built.

In this study, inspired by many natural surfaces, we proposed a 3-level hierarchical surface design that consists of the cone, cuticle, and wrinkle structures. The SA/V ratio for each level was modeled, and geometric and manufacturing constraints were defined as functions of design parameters. The geometric error caused by the voxel arrangement along the contour of each level design was modeled. In addition, a process flowchart for TPP process optimization was proposed for the 3-level design. To validate the effectiveness of the proposed surface structure design on tuning surface functionalities, the contact angle and antireflection properties of the fabricated samples were characterized.

The rest of this paper is organized as follows. In Sec. 2, the 3-level surface structure design is proposed, and the SA/V ratio for each level is modeled. In Sec. 3, methodologies, including the modeling of constraints, geometric error, and the process flowchart, are presented. Case studies and results are discussed in Sec. 4, including model validation and functionality study. Finally, in Sec. 5, conclusions and future work are discussed.

2 Design and Methods

2.1 Hierarchical Structures in Nature. As summarized in Table 1, we calculated the SA/V ratios of varied common geometries with the same surface area (200 mm^2). We found that the cone structure, especially with a large AR, exhibits one of the highest SA/V ratios. This finding agrees well with numerous nano/micro-scale patterns observed in bio-organisms. For example, hierarchical cone structures enable anti-bacterial functionality, as shown in Fig. 1(*a*). Kelleher et al. systematically studied the correlation between the bactericidal properties and the surface topology of various cicada wing surfaces with conical microstructures [46]. The bactericidal properties of two cicada wings species were characterized by the dead/alive cell ratio on their surfaces with conical structures. High dead/alive cell ratios were observed on the wings of *Megapomponia intermedia* (SA/V $\approx 0.053\ nm^{-1}$) compared with the *Ayuthia spectabile* species (SA/V $\approx 0.050\ nm^{-1}$), suggesting a strong correlation between the bactericidal properties and the hierarchical surfaces with high SA/V ratio [46].

Moreover, some other biological organisms, such as the surface of the lotus plant leaves, show patterned nano/micro-scale conical structures with cuticles, as shown in Fig. 1(*b*). The lotus plant leaves covered with conical structures and cuticles are superhydrophobic (161 deg equilibrium contact angle), while some lichens and mosses with no such surface structures are superhydrophilic. Studies by Wenzel confirmed that the conical surface structures covered with wax cuticles play a vital role in developing the superhydrophobicity [47]. Additionally, Schulte et al. studied the correlation between the hydrophobicity and the surface topology of various hierarchically structured flower petal surfaces [15]. A high contact angle of the water droplet was observed on the petals of *Viola tricolor* (CA $\approx$ 169 deg; SA/V $\approx 0.373\ \mu m^{-1}$) compared with the *A. spectabile* species (CA $\approx$ 136.4 deg; SA/V $\approx 0.31\ \mu m^{-1}$), suggesting an enhancement in the hydrophobicity can be achieved by hierarbchical surfaces with conical surface structures.

Table 1 SA/V of common geometries (SA = 200 mm^2)

	Various Geometries								
	Cylinder	Sphere	Capsule	Octahedron	Cube	Cone (Low AR)	Tetrahedron	Disc	Cone (High AR)
Characteristic Length (mm)	318.37	3.99	2.82	7.60	5.77	17.98	10.75	7.62	126.89
Volume (mm^3)	316.1	266.03	235.14	206.80	192.45	169.40	146.23	41.42	33.20
Base Radius (mm)	0.1	N/A	5.64	N/A	N/A	3	N/A	3	0.5
SA/V Ratio (mm^{-1})	0.633	0.75	0.85	0.97	1.04	1.18	1.37	4.83	6.02

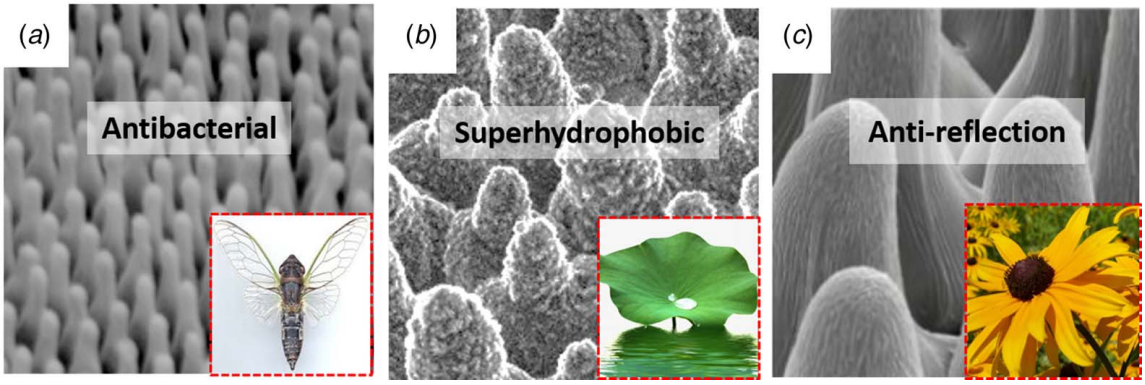

Fig. 1 Hierarchical surface structures in nature: (*a*) cicada wing: cone [14]; (*b*) lotus leaf: cone with cuticles [9]; and (*c*) rudbeckia: cone with surface wrinkles [16]

In addition to the conical structures and cuticles, some natural surfaces also integrate wrinkles to further increase the SA/V ratio and enhance some functionalities. Schulte et al. investigated the influence of wrinkle surface structures on the ultraviolet (UV) light reflection [16]. Their study investigated different flower surfaces consisting of conical hair-papilla with vertical surface wrinkles, as shown in Fig. 1(*c*). It was found that the reflection of the papillae of *Bidens ferulifolia* (SA/V $\approx 0.239\ \mu m^{-1}$) is 1.2%, while the reflection of the papillae of *Rudbeckia fulgida* (SA/V $\approx 0.194\ \mu m^{-1}$) is 0.8%. The difference in antireflection properties of *B. ferulifolia* and *R. fulgida* is mainly caused by surface morphologies, especially the height of conical papilla and vertical surface wrinkles. According to these studies, varied functionalities can be enhanced or even enabled by hierarchical conical structures with high SA/V ratios and proper combinations of cuticles and surface wrinkles.

2.2 Proposed 3-Level Hierarchical Surface Structure Design. Inspired by these biological systems, a 3-level hierarchical surface structure design is proposed in this study, as shown in Fig. 2. *Level-1* consists of a series of nonoverlapping conical structures ($P > 2R_2$) with constant pitch distance *P*. *Level-2* consists of numerous down-scaled *Level-1* features (i.e., cuticles) on the cone surface ($r_{c2} < R_1$). Inspired by cicada microstructure, the aspect ratio of cone and cuticles were kept as same ($\alpha = \alpha_c$). *Level-3* is based on both *Level-1* and *Level-2*, with textures such as surface wrinkles uniformly implemented on the cuticle surface. Inspired by many natural structures with varied functionality, including *V. tricolor*, *Aztekium ritteri*, Dahlia, *R. fulgida,* and *B. ferulifolia* [15,16,18], and considering the ease of manufacturing, vertical wrinkles were selected. Here, to study the influence of design parameters in each level on the surface morphology, the corresponding SA/V ratio is mathematically modeled as follows.

2.2.1 Level-1: Cone. As illustrated in Fig. 2(*a*), *H*, R_1, and R_2 are the height, radius of small, and big circular end of the cone, respectively. The pitch distance is *P*. *N* is the number of nano/micro-cones on a substrate surface with a length of *L* (mm) and width of *W* (mm). The volume for *Level-1* design consisting of *N* cones can be calculated according to the generalized equation of frustum:

$$V_1 = N\left(\frac{1}{3}\,\pi\, H[R_1^2 + R_2^2 + R_1R_2]\right) \tag{1}$$

And the conical structured surface area for *Level-1* design can be calculated as

$$SA_1 = N\,(\pi\,[(R_1 + R_2)S + R_1^2]) \tag{2}$$

where *S* is the slant height of the cone, *N* is a function of the pitch distance *P,* and the substrate surface area covered by the conical structures, $N = \left(\frac{L}{P} - 1\right)\left(\frac{W}{P} - 1\right)$.

2.2.2 Level-2*: Cone With Cuticles.* As illustrated in Fig. 2(*b*), h_c, r_{c1}, $r_{c2,}$ and n_c are the height, radius of small and big circular end of the cuticle, and the number of cuticles on each conical structure, respectively. The number of cuticles n_c ranges from 0 to $((R_1 + R_2)S)/r_{c2}^2$ for the closely packed distribution on the surface of the cone structure. The volume of *Level-2* design with *N* cones and n_c cuticles on each cone can be calculated as

$$V_2 = \frac{1}{3}N\pi[H(R_1^2 + R_2^2 + R_1R_2) + n_ch_c(r_{c1}^2 + r_{c2}^2 + r_{c1}r_{c2})] \tag{3}$$

The surface area of *Level-2* design is

$$SA_2 = N[n_c\pi[(r_{c1} + r_{c2})S_c + r_{c1}^2] + \pi\,[(R_1 + R_2)S + R_1^2 - n_cr_{c2}^2\,]\,] \tag{4}$$

where S_c is the slant height of the cuticle.

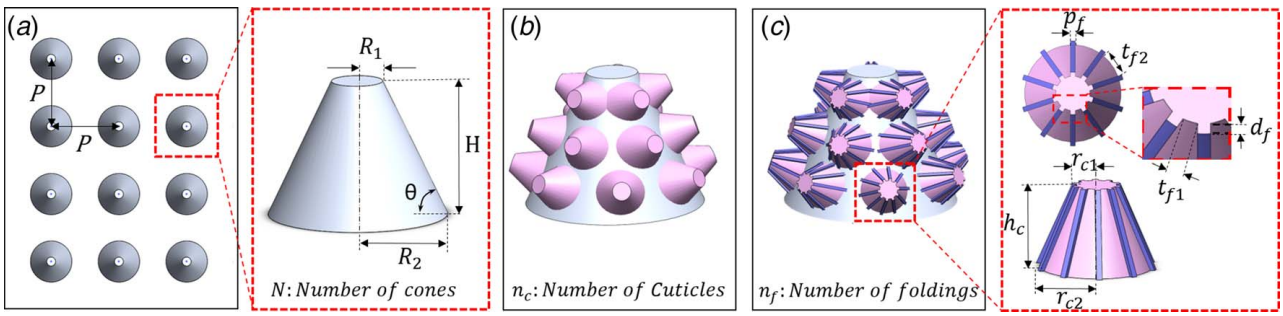

Fig. 2 Bio-inspired 3-level hierarchical design: (*a*) *Level-1:* cone; (*b*) *Level-2*: cone with cuticles; and (c) *Level-3*: cone with cuticles and surface wrinkles

2.2.3 Level-3*: Cone With Cuticles and Surface Wrinkles.* As illustrated in Fig. 2(*c*), the width, height, and the number of wrinkles on each cuticle are denoted as p_f, d_f, and n_f, separately. A higher SA/V ratio can be achieved by keeping the gap between wrinkles on the top face of a cuticle greater than the width of a single wrinkle, i.e., $t_{f1} \geq p_f$. The height of the wrinkle is finite, i.e., $d_f \leq r_{c1} - (t_{f1} \cdot n_f / 2\pi)$.

Hence, the gap between wrinkles at the bottom face of a cuticle t_{f2} can be written as

$$t_{f2} = t_{f1}\left[\frac{2\pi r_{c2} - p_f n_f}{2\pi r_{c1} - p_f n_f}\right] \tag{5}$$

The reduction in volume due to the grooves between wrinkles can be modeled as

$$V_f = n_f d_f S_c\left(\frac{t_{f2} + t_{f1}}{2}\right) \tag{6}$$

Substituting (6) into (3) yields

$$V_3 = \frac{1}{3}N\pi[H(R_1^2 + R_2^2 + R_1R_2) + n_c h_c(r_{c1}^2 + r_{c2}^2 + r_{c1}r_{c2})] - n_f d_f S_c\left(\frac{t_{f2} + t_{f1}}{2}\right) \tag{7}$$

And, an increase in surface area caused by the wrinkles can be calculated as

$$SA_f = 2n_f d_f S_c \tag{8}$$

Substituting (8) into (4), we can get the surface area for *Level-3* design as

$$SA_3 = N\left[n_c\,\pi\left[(r_{c1} + r_{c2})S_c + r_{c1}^2\right] + \pi\left[(R_1 + R_2)S + R_1^2 - n_c r_{c2}^2\right] + 2n_f d_f S_c\right] \tag{9}$$

3 Two-Photon Polymerization Fabrication of the Hierarchical Surface Structure

3.1 Experimental Setup and Materials. TPP fabrication of the designed hierarchical structures was carried out with a Photonic Professional GT (Nanoscribe GmbH, Germany) system. This setup mainly consists of three portions: (1) the laser system, (2) the scanning system, and (3) the stage positioning system. In the laser system, a femtosecond laser with 100 fs pulses delivering at 80 MHz repetition rate (center wavelength: 780 nm) was equipped as the excitation source. The typical printing range of the given setup is $300 \times 300 \times 300\ \mu m^3$, and the writing volume can be up to $100 \times 100 \times 8\ mm^3$. According to the specification, the printer has a 200 nm smallest feature size, 500 nm *XY* resolution, and 1500 nm Z resolution**.**

IP-S (Nanoscribe GmbH, Germany), a photocurable negative-tone resin, was tested in this study. The resin is specifically developed for the TPP process. A 700 μm thick ITO-covered glass ($25 \times 25\ mm^2$) was used as the substrate in all experiments. A 25×1.4 NA microscope objective lens was utilized to tightly focus the laser beam into the volume of liquid resin. In all the experiments, 80% of the incident laser power (P) and 100% of the writing speed (W) were used to prevent over-exposure. A CCD monochrome microscope camera (AxioCam MRM) was mounted on the microscope system to monitor the fabrication in real-time.

3.2 Fabrication Process. Figure 3 illustrates the typical procedure to fabricate the proposed hierarchical nanostructured surface using the TPP setup. A computer-aided design (CAD) model was first created. 3 μL of IP-S photoresist was carefully deposited in the center of the ITO coated glass substrate. By using an appropriate holder, the photoresist droplet was then transferred to the TPP system. A voxel model was constructed using Describe (Nanoscribe GmbH, Germany) software by adjusting the slicing (d_s) and hatching (d_h) distance, as illustrated in Fig. 4. According to the voxelized digital file, the hierarchical structures were printed in a voxel-by-voxel way, as shown in Figs. 4(*c*) and 4(*d*). In general, the printing quality is highly dependent on the size of the three-dimensional voxel (*XY* and *Z* resolution). It should be noted that the smallest feature size is also one of the critical factors in determining the printing quality, which is usually characterized by the smallest printable size of a single droplet within a voxel [48].

After printing, the samples were placed in a SU-8 (MicroChem Corp., Westborough, MA) bath for 9 min to remove any unsolidified photoresist, as illustrated in Fig. 3(*c*). Subsequently, they were then transferred to an IPA (Sigma-Aldrich, MO) bath for another 2 min. Afterward, the samples were thoroughly dried at

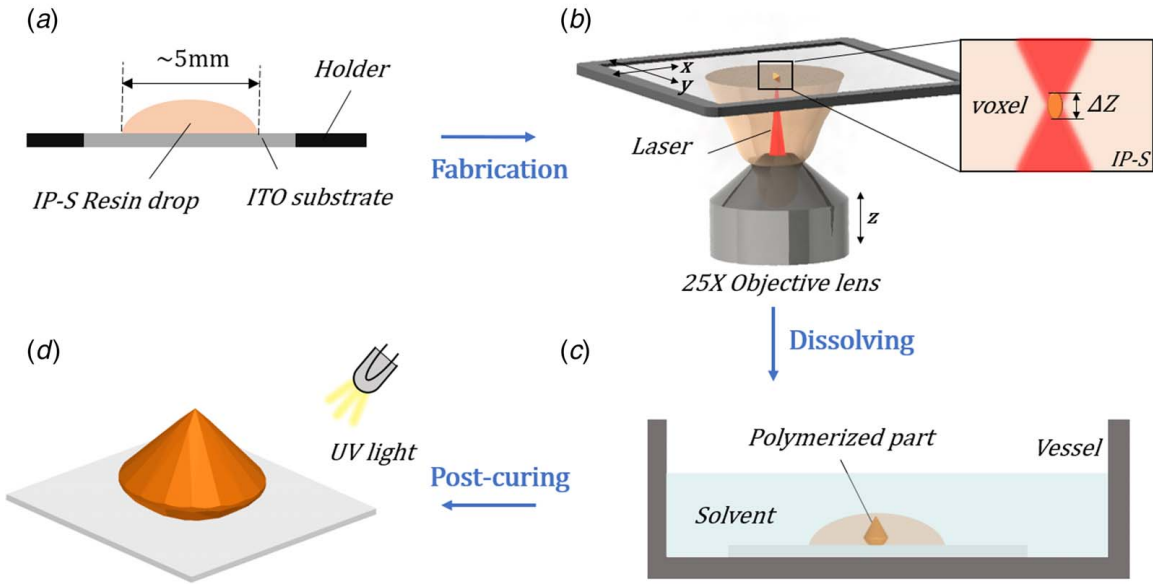

Fig. 3 Schematic illustration of the TPP fabrication procedure: (*a*) sample preparation, (*b*) TPP fabrication, (*c*) dissolving in SU-8 and IPA solution, and (*d*) UV light curing

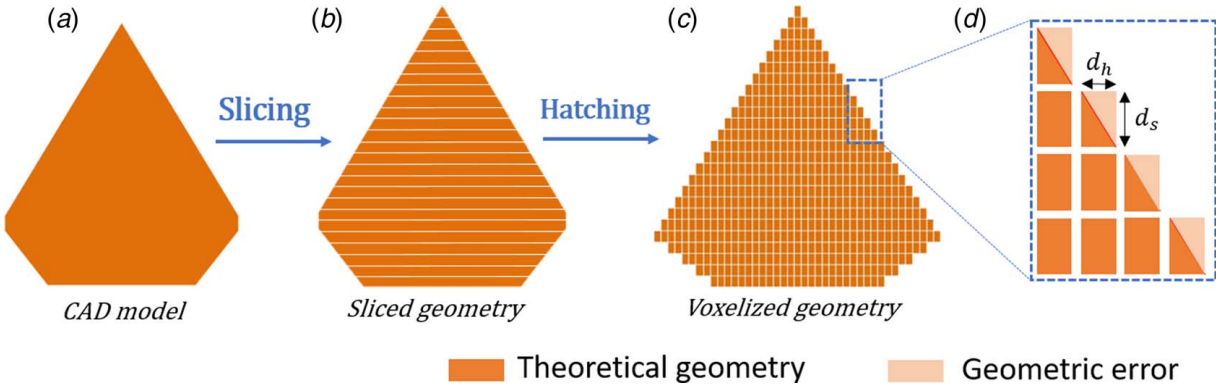

Fig. 4 Voxelization in the TPP process: (*a*) actual geometry, (*b*) geometry after slicing, (c) geometry after hatching, and (*d*) voxel arrangement based on *XY* and *Z* resolutions

room temperature to evaporate the remaining IPA. Finally, as illustrated in Fig. 3(*d*), samples were placed in the irradiation chamber for heat curing (Dymax BlueWave 200, Torrington, CT) and exposed to UV light with an intensity of 17,000 mW/cm^2 for 45 s before any experimental characterizations.

3.3 Manufacturing Constraints for the Hierarchical Surface Structure Design. We investigated manufacturing constraints for the typical TPP fabrication of the proposed hierarchical structures. In most AM techniques, especially the TPP process, several typical manufacturing constraints are (1) smallest printable feature size a, (2) XY resolution ΔX and ΔY (ΔX equals to ΔY in most cases), and (3) Z resolution ΔZ.

3.3.1 Level-1*: Cone.* Figure 5(*a*) illustrated the proposed 3-level hierarchical surface structure design with a cone angle of θ, which is a critical variable influencing the voxel arrangement in the TPP process, and hence, printing quality. Figure 5(*b*) illustrates design parameters and voxel arrangements for the cone structure in *Level-1* design. Based on the voxel arrangement, the manufacturing of the cone structure is mainly limited by XY and Z resolutions (ΔXY and ΔZ) of the TPP process. Accordingly, to use the TPP technique to fabricate the *Level-1* surface structure design, the cone design should satisfy the following equations:

$$R_2 = k_1 \Delta X \tag{10}$$

$$R_1 = k_2 \Delta X \tag{11}$$

and

$$H = k_3 \Delta Z \tag{12}$$

where k_1, k_2, and k_3 are integers and should satisfy $k_3 > k_1 > k_2$.

3.3.2 Level-2*: Cone With Cuticles.* The voxel arrangement of cuticles in *Level-2* design is illustrated in Fig. 5(*c*). The cuticles are covering the curved surface of the cone. The geometry of the cuticle is hence highly related to the cone angle θ. The manufacturing constraints for fabricating these overhanging cuticles are

$$r_{c1} = k_4 \frac{\Delta X}{\cos\theta} \tag{13}$$

and

$$h_c = k_5 \frac{\Delta Z}{\cos\theta} \tag{14}$$

where k_4 and k_5 are integers with $k_5 > k_4$.

3.3.3 Level-3*: Cone With Cuticles and Wrinkles.* Figure 5(*d*) illustrates the arrangement of voxel for wrinkle structure in *Level-3* design. The smallest wrinkle width p_f and groove height d_f are limited to the TPP smallest printable feature size a, mostly determined by the laser. The feature size a is usually characterized by the smallest printable size of a single droplet. To fabricate defect-free wrinkles, the wrinkle width p_f and height d_f should be greater than the smallest printable feature size of the TPP printer

$$p_f > a \text{ and } d_f > a \tag{15}$$

3.4 Printing Geometric Errors. In the TPP process, the printing geometric error depends on the voxel positions on the contour of the geometry. As a result, the fabricated part shows a ragged contour. It is noteworthy that the surface quality of the fabricated geometry in the TPP process markedly depends upon the orientation of the model and voxel dimension. This section aims to study the influence of voxel arrangements of the proposed 3-level hierarchical structures on printing geometric errors, as shown in Fig. 5, and develop a generalized model to predict the geometric error for each level.

In Figs. 5(*b*)–5(*d*), voxel arrangements for three levels and their respective theoretical printing surface profiles, characterized by cone angle θ, are illustrated. It can be seen that the voxel arrangement influences the model surfaces: each step can be considered as a triangle. The side lengths of the triangle can be characterized, dependent upon the number of voxels in the X and Z direction, voxel size, and cone angle, as shown in Fig. 5(*e*). The largest distance between the printed ragged contour and the designed contour is denoted as ε, representing the printing geometry error. It is shown that ε depends upon the orientation of the profile shape in each level. Hence, the printing geometric error is trigonometrically obtained by

$$\varepsilon_i = n d_s \sin\beta \tag{16}$$

where n is the number of voxels along X direction and β is a function of the cone angle θ and design level $i \in [1,3]$ as follows:

$$\beta = \begin{cases} \theta, & i = 1 \\ 2\theta, & i = 2 \\ \theta + 90 \text{ deg}, & i = 3 \end{cases} \tag{17}$$

The 3-level surface structure design is characterized by various geometric and manufacturing parameters, including the size of the substrate, the number of structures in each level, pitch distance, and printing resolution. These parameters can be optimized to achieve a specific goal, such as the desired SA/V ratio with the smallest printing error while meeting design and manufacturing constraints. The proposed process flowchart is shown in Fig. 6.

The surface structure design optimization process begins with an initialization step defining the targeted application with the desired SA/V ratio, the printing geometric error, the constraints based on Eqs. (10)–(15), and setting the TPP process and initial design parameters. Predicted SA/V ratio and geometric error are then computed

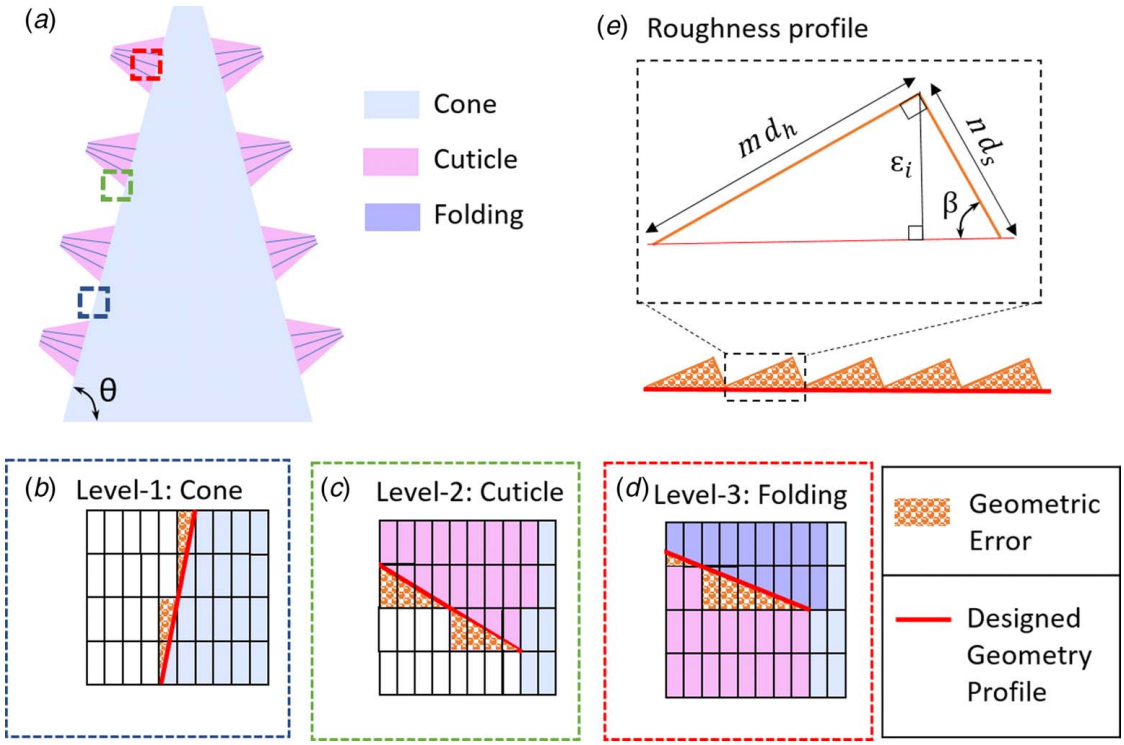

Fig. 5 Schematic of printing geometric error due to the voxel-by-voxel manufacturing mechanism: (*a*) schematic drawing of 3-level design; (*b*)—(*d*) voxel arrangements for *Level-1, Level-2, and Level-3* design, respectively; and (*e*) illustration of the printed ragged profile comparing to the profile of the designed geometry

using Eqs. (1)–(9) and Eqs. (16) and (17), respectively. The difference between the desired and predicted values of SA/V ratio (x_1) and geometric error (x_2) are calculated and used to evaluate the objective function for the given application. If x_1 and x_2 are greater than a certain threshold (5% used in this study), then design parameters H, n_c, and n_f must be updated based on the goal [49]. For instance, if the goal is to increase the SA/V ratio, then we need to reduce H and increase n_c and n_f. The process goes on iteratively until x_1 and x_2 are lesser than the threshold, e.g., 5% used in the test case in this study. Once the design parameter settings satisfy the objective function, the 3-level hierarchical structure is designed and then printed. Finally, the printed structure is characterized to validate the design and tested for the target application.

4 Results and Discussion

4.1 3d Printed 3-Level Hierarchical Structures. Most natural hierarchical structures, including Lotus leaf, Cicada wing, and Rudbeckia exhibit a 10–50 μm cone size and a 10–100 μm pitch distance. To mimic those bio-structures, the sizes of the hierarchical surface structures tested in this work are within these

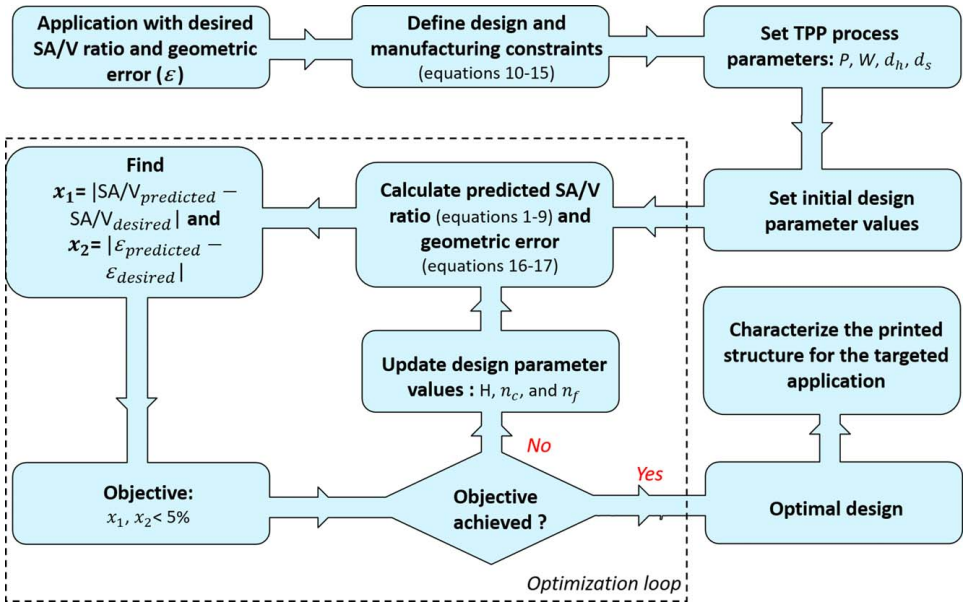

Fig. 6 Overview of the proposed process flowchart for 3-level design

Table 2 Optimal design parameter settings and predicted properties

Optimal design parameters				
L-1	*L-2*	*L-3*	Predicted values and error	
$P = 64\ \mu m$	$r_{c1} = 1.25\ \mu m$	$p_f = 0.5\ \mu m$	$SA/V_{desired} = 4.60\ \mu m^{-1}$	$\epsilon_{desired} = 0.05\ \mu m$
$R_1 = 10\ \mu m$	$r_{c2} = 2.5\ \mu m$	$d_f = 0.5\ \mu m$	$SA/V_{predicted} = 4.54\ \mu m^{-1}$	$\epsilon_{predicted} = 0.048\ \mu m$
$R_2 = 50\ \mu m$	$h_c = 5\ \mu m$	$t_f = 0.8\ \mu m$	$x_1 = 1.3\%$	$x_2 = 4\%$
$H = 80\ \mu m$	$n_c = 88$	$n_f = 6$		
$\theta = 76$ deg	$\alpha_c = 4$			
$\alpha = 4$				
$N = 9$				

ranges. The design parameter settings used in this test case study were based on the proposed process flowchart, the geometric constraints, and manufacturing constraints developed in Eqs. (1)–(17). The proposed process flowchart was applied to find the optimal design parameter settings for printing surface structures with the target SA/V ratio and ϵ as 4.6 μm^{-1} and 0.05 μm, respectively. From the results summarized in Table 2, it can be seen that $x1$ and $x2$ are predicted to be 1.3% and 4%, respectively.

To validate the design, the fabricated 3-level hierarchical microstructures were characterized by scanning electron microscope (SEM) imaging, as shown in Fig. 7. The specimens were coated by 6 nm platinum particles before SEM imaging to avoid charging. Afterward, the samples were observed under a scanning electron microscope (JEOL JSM-IT500HR FESEM) using its high vacuum mode. The spot size and the accelerating voltage of the SEM were 4.0 and 5 kV, respectively. The SEM device has built-in measurement functions with the smallest measurable feature size as 8 nm. Figures 7(*a*)–7(*l*) show the SEM images of the TPP printed 3-level surface structure design at various magnifications. By analyzing the SEM images, the dimensions of the printed structures were measured. The corresponding feature size and the pitch distances of the cone structures in *Level-1* were measured as 50 μm and 64 μm, respectively. The height and diameter of cuticle structures in *Level-2* were 5 μm and 5 μm, respectively. The width and height of wrinkles in *Level-3* were 0.5 μm and 0.5 μm. It can be seen that the measured surface structure dimensions agree well with the design parameter settings, allowing us to make conclusions about the high degree of printing accuracy. It is also worth mentioning that the printed structures show well-defined defect-free features and hierarchical geometries with excellent surface quality.

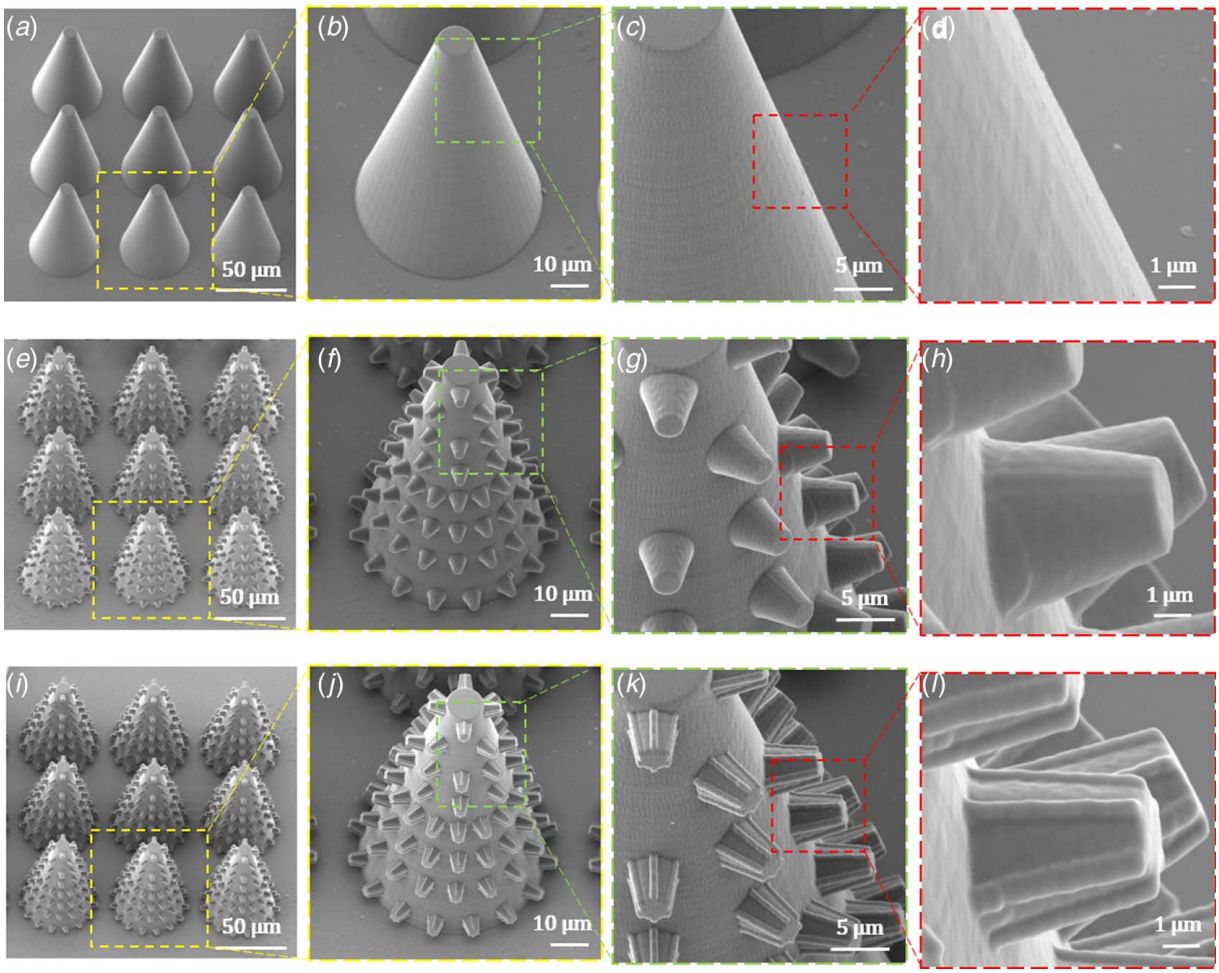

Fig. 7 SEM images of printed surface structures for: (*a*)–(*d*) *Level-1* design; (*e*)–(*h*) *Level-2* design; and (*i*)–(*l*) *Level-3* design with the design parameter settings listed in Table 2

Table 3 Design of experiments table and experimental data

Experiment No.	c	l	H (μm)	n_c	n_f	r (μm^{-1})	CA (deg)
1	1	0	0	0	0	0.052	63
2	1	1	10	0	0	0.330	72.04
3	1	1	15	0	0	0.299	76.3
4	1	1	20	0	0	0.286	81.37
5	1	2	20	8	0	0.346	84.7
6	1	2	20	13	0	0.377	93.9
7	1	2	20	18	0	0.399	92.53
8	1	3	20	18	3	0.404	93.7
9	1	3	20	18	6	0.406	94.31
10	1	3	20	18	8	0.408	97.18
11	2	0	0	0	0	0.052	90.3
12	2	1	10	0	0	0.330	89.03
13	2	1	15	0	0	0.299	90.4
14	2	1	20	0	0	0.286	102.98
15	2	2	20	8	0	0.346	114.22
16	2	2	20	13	0	0.377	122.2
17	2	2	20	18	0	0.399	126.25
18	2	3	20	18	3	0.404	127.55
19	2	3	20	18	6	0.406	128.61
20	2	3	20	18	8	0.408	138.5

4.2 Measurement and Analysis of Surface Wettability. Here, we investigated the influence of manufacturing-constrained design parameters, including the cone height H of *Level-1*, the number of cuticles n_c of *Level-2*, and the number of wrinkles n_f of *Level-3* on the wettability of the printed patterned surfaces. Nine hierarchically structured surfaces with different H, n_c, and n_f values (H: 10, 15, 20 μm, n_c: 8, 13, 18 μm, n_f: 3, 6, 8, respectively) were fabricated using the TPP process. The design of experiments and experimental data are shown in Table 3.

As shown in Table 3, for a higher level design, the parameter setting which gives the optimum experimental result in the previous level is used. For instance, in L-1 design, $H = 20$ gave the highest contact angle. Therefore, in L-2 design, all surface structures are designed with $H = 20$ and the remaining two levels of H were disregarded in the L-2 design investigation. In the study of L-2 design, it was found that $n_c = 18$ resulted in the optimum experimental result. Therefore, all L-3 designs used $n_c = 18$. Other design parameter settings were fixed as follows: in *Level-1* design, for the cone, the top radius was 5 μm, and the base radius was 10 μm. In *Level-2* design, for the cuticle, the top radius, base radius, and height were 1.25 μm, 2.5 μm, and 5 μm, respectively. In *Level-3* design, both the width and height of wrinkles were 0.5 μm. The printed surface consists of 45 by 45 microstructures, and the center-to-center distance between micro-cones is 45 μm [50].

The contact angle of the printed hierarchically structured surface was measured using a dynamic contact angle measuring device (DCAT-25, DataPhysics Instruments), which has a measuring range of 0–180 deg with a measurement accuracy of 0.01 deg. Deionized water droplets of approximately 1.5 μL were carefully deposited onto the sample surface using a pipette. The droplet was recorded in real-time using the DCAT-25 software, and contact angles were measured using the ImageJ software. All the experiments were conducted under a temperature of 70 °F and humidity of 45%. As shown in Table 3 and Fig. 8(*a*), the contact angles of the printed hierarchically structured surfaces from *smooth* to *Level-3* design improved from 63 deg to 100 deg (orange bar). Experimental results show that the proposed hierarchical surface structures can effectively change the naturally hydrophilic IP-S surface to hydrophobic.

In addition, it has been reported that the deposition of the Parylene-C layer can further improve the hydrophobicity of the surface [51]. To test the effect of Parylene-C coated surface structure, a thin layer (≈100 nm) of Parylene-C was coated on all samples using a vacuum deposition system (PDS 2010 Labcoater, Speciality coating system, Indianapolis, IN). The TPP printed samples were first cleaned using the IPA solution for 2 min before Parylene-C coating. In the deposition chamber, the vaporized Parylene-C was deposited onto the hierarchical surface structure at 680 °C. As summarized in Fig. 8(*a*), the static contact angles of the Parylene-C coated hierarchically structured surfaces were in the range of 90–138 deg (right bar).

Evaluations of wetting characteristics in different coated structures with varied hierarchy (i.e., smooth, *Level-1* to *Level-3*) and varied SA/V ratios are summarized in Fig. 8(*b*). The SA/V ratio of each level of design was calculated using Eqs. (1)–(9). From detailed investigations of contact angles in four samples varied by increasing the SA/V ratio, one can observe that an increase in the SA/V ratio led to an increase in contact angle. By using a 3-level hierarchical structure, the contact angle increased to 138 deg. This reflects that the structured surface with a large SA/V ratio was efficient in enhancing the hydrophobicity.

Furthermore, using the first-order regression analysis, a mathematical predictive model for contact angle was developed according to the analysis of the experimental results, as shown in Table 3:

$$\mathrm{CA} = 35.44 + 28.10\,c - 2.32\,l + 1.139\,H + 1.320\,n_c + 0.914\,n_f - 21.4\,r \tag{18}$$

where c denotes the coating type with 1 for no coating and 2 for coated, l denotes the hierarchy level of the design with possible values of 0, 1, 2, and 3, and r denotes the SA/V ratio.

In order to evaluate the goodness of fit of the developed contact angle regression model, the fitted regression model Eq. (18) was

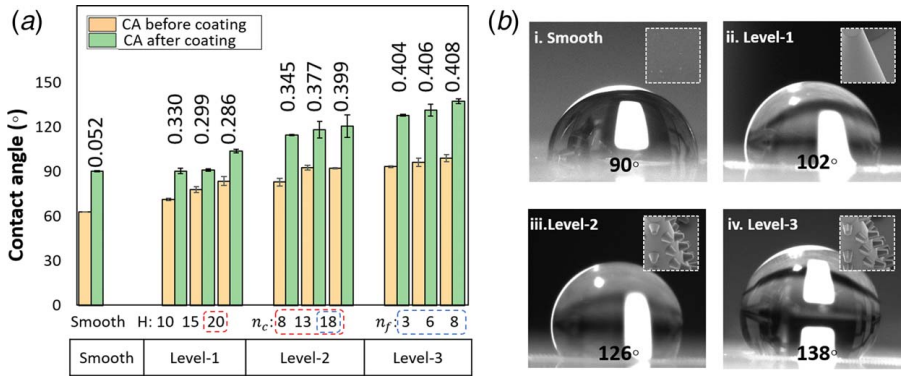

Fig. 8 Contact angles of the surfaces with different microstructures: (*a*) the contact angle measurements conducted before and after Parylene-C coating and (*b*) corresponding water droplet images for surfaces with SA/V ratio (i) 0.052 μm^{-1}, (ii) 0.286 μm^{-1}, (iii) 0.399 μm^{-1}, and (iv) 0.408 μm^{-1}

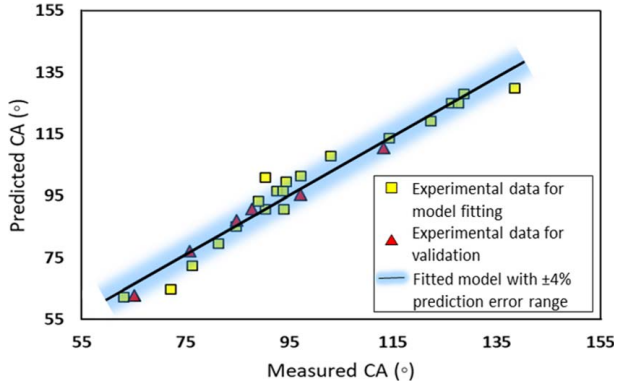

Fig. 9 Predicted versus measured values of contact angle

plotted as a function of the experimental data, as shown in Fig. 9. It shows that the fitted model agrees well with measured experimental data (less than 5% error), verifying the adequacy and goodness of fit of the developed model. Moreover, to validate the model further, six new confirmation tests were performed with new experimental conditions. Table 4 summarizes the experimental conditions, the experimental data, the predicted data computed from the regression model, and the prediction error. The experimental values are found to be in good agreement with predicted values with an average prediction error of ~2.67%. As shown in Fig. 9, the six validation experimental data were plotted as red triangles, and they all fall within the 4% prediction error range (denoted by the translucent zone in Fig. 9).

4.3 Antireflection Properties of the 3-level Design. Antireflection is an important property for many natural structures, including the moth eye and fish scale. Moreover, antireflection is widely used in a variety of engineering applications, including solar cells and optoelectronic devices [52]. To further validate the potential of the proposed hierarchical surface structure, in this study, we investigated the influence of the 3-level design on the antireflection property of the printed surfaces over a broad range of wavelengths (350–800 nm). According to previous literature [16], the height of the *Level-1* cone has an influence on the reflection value; therefore, the comparison was made between *Level-1*, *Level-2,* and *Level-3* hierarchically structured surfaces with identical values of the common *Level-1* cone height. Three hierarchically structured surfaces, one for each level, were designed with $H = 20\ \mu$m, $n_c = 18$, and $n_f = 8$ and fabricated using the developed method.

The spectral measurements were performed using a single-beam UV-VIS spectrophotometer (V721, Shanghai Yoke Instruments Co., Ltd., China). A smooth polymer surface was used as a reference. Experimental results are plotted in Fig. 10(*a*). It shows that the 3-level hierarchically structured surfaces exhibit significantly lower reflection values than the smooth reference surface. The reduction of the reflection by 3-level surface structures can be seen through the entire range of wavelengths from 350 nm to 800 nm measured in this experiment. As the level increased, the reflection value significantly reduced. For example, at 700 nm wavelength, while the smooth reference (SA/V = 0.052) reflected about 11% of the incoming light, the *Level-1* (SA/V = 0.286) surface demonstrated 7.8% reflection. With the surface structure hierarchy level increased, the reflection of *Level-2* (SA/V = 0.399) surface reduced to 3.7%, followed by the *Level-3* (SA/V = 0.408) surface with a reflection as low as 1.7%. Figure 10(*b*) shows the average reflection of the smooth and the 3-level hierarchically structured surfaces in 4 wavelength ranges, 400–500 nm, 500–600 nm, 600–700 nm, and 700–800 nm. It shows that the average values of the measured reflection of *Level-1*, *Level-2*, and *Level-3* surface in the four wavelength ranges were all lower than 12%, 9.5%, and 8%, respectively, compared with the smooth surface (> 12%). In particular, in the 700–800 nm range, a light reflection reduction of 83% was demonstrated, with the average reflection measurement reduced from 12.4% of the reference surface to 2.0% of the *Level-3* surface. The addition of micro-cuticles and nano-wrinkles induces strong geometrical light trapping effects in

Table 4 Experimental validation

							Response		
Exp. no.	c	l	H (μm)	n_c	n_f	r (μm^{-1})	Experimental CA	Predicted CA	ε (%)
1	1	1	8	0	0	0.360	65.1	62.7	3.67
2	1	2	12	10	0	0.403	75.82	77.14	1.74
3	1	2	15	15	0	0.405	84.79	87.10	2.72
4	1	3	22	14	5	0.433	97.18	95.41	2.14
5	1	3	17	30	6	0.488	113.2	110.57	2.32
6	2	1	8	0	0	0.360	87.78	90.80	3.42

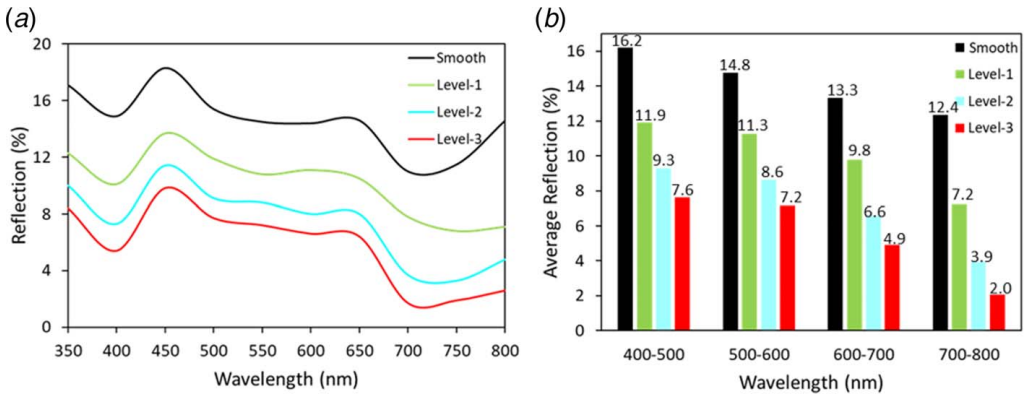

Fig. 10 Reflection spectra: (*a*) percent reflection of light by smooth and 3-level surfaces in the wavelength range of 350–800 nm and (*b*) average reflection in different wavelength ranges

the *Level-2* and *Level-3* surfaces, thereby resulting in stronger antireflection properties compared with the *Level-1* surface and the smooth surface. The results agree well with the findings in the work presented by Schulte et al. [16] and Ahn et al. [53]. It also indicates the feasibility of the proposed 3-level hierarchical surface structure design for tuning different functionalities, including wettability and antireflection functions.

5 Conclusion

In this paper, inspired by many natural surfaces with cone, cuticle, and wrinkle structures, we proposed a 3-level hierarchical surface structure design. The SA/V ratio for each level was modeled, and geometric designs were mathematically defined. A TPP technology was investigated for fabricating the proposed surface structures. The manufacturing geometric error caused by the voxel-by-voxel printing mechanism of the TPP process was modeled. In addition, a process flowchart was developed to identify the optimal design parameter settings of the proposed 3-level hierarchical structures based on the target functionality, desired SA/V ratio, and printing geometric error. Surfaces with hierarchical structures were designed using the flowchart and fabricated by the TPP process. SEM imaging technique was used to experimentally observe and measure the printed surfaces. It was worth noting that the observed feature sizes in all sample surfaces agreed well with the digital model designs. The printed structures showed well-defined defect-free features and hierarchical geometries with a high degree of printing accuracy.

To demonstrate the potential applications of the proposed hierarchical surface structures, the influence of the surface structure hierarchy and SA/V ratio on the wettability and antireflection properties was investigated. It was found that the proposed hierarchical surface structure design could effectively reduce the wettability and could even change a naturally hydrophilic surface to a near-superhydrophobic surface. Besides, the proposed hierarchical surface structures can effectively work as strong geometrical light trapping structures and hence significantly enhance the antireflection property. By adjusting the surface structure design parameter settings, the antireflection property could be tuned within a wide wavelength range of 350–800 nm. Compared with the smooth surface reference, an antireflection enhancement of $>80\%$ was observed in the *Level-3* hierarchically structured surface sample. The results indicated that by using our proposed design and process planning approach, surface structures with a wide range of functionalities can be produced.

Although TPP provides a relatively efficient method to fabricate the proposed hierarchical surface structures, its material choice is limited. Only a few photosensitive resins are printable by TPP process. Limited by the material properties of the TPP printable resins, the nano/micro-structured surfaces printed by TPP could not withstand large mechanical forces and thus may have limited life time, especially for applications in harsh environments. Various approaches have been proposed to protect nano/micro-structured surfaces. For example, protective coatings that possess high friction coefficient were shown to be effective for increasing the wear life of microstructures [54,55]. Besides, successful manufacturing of fiber/particle-reinforced polymer composites with TPP processes have been reported in literature [37,56–58]. With functional composites as feedstock for TPP, productions of hierarchically nano/micro-structured surfaces with a wider range of programmable functionalities and superior mechanical properties would be possible.

To conclude, we believe that this study could help design and engineering of biomimic hierarchical surface structures and promote inventions of novel substrates for various applications, including microfluidics, energy, optics, and interface. Future work could extend the proposed hierarchically structured surface design to multi-material hierarchically structured surfaces (e.g., comprising both soft and hard materials), by utilizing multi-material manufacturing approaches which can fabricate parts with spatially varied material compositions, for a wider range of advanced applications.

Acknowledgment

This study is based upon work partially supported by the National Science Foundation under Grant No. 1663399. The authors are thankful for the funding of this project and the service from the UIC Nanotechnology Core Facility.

Conflict of Interest

There are no conflicts of interest.

Data Availability Statement

The datasets generated and supporting the findings of this article are obtainable from the corresponding author upon reasonable request. The authors attest that all data for this study are included in the paper.

References

[1] Gaikwad, A. M., Whiting, G. L., Steingart, D. A., and Arias, A. C., 2011, "Highly Flexible, Printed Alkaline Batteries Based on Mesh-Embedded Electrodes," Adv. Mater., **23**(29), pp. 3251–3255.

[2] Hoth, C. N., Choulis, S. A., Schilinsky, P., and Brabec, C. J., 2007, "High Photovoltaic Performance of Inkjet Printed Polymer: Fullerene Blends," Adv. Mater., **19**(22), pp. 3973–3978.

[3] Cooney, C. G., Chen, C.-Y., Emerling, M. R., Nadim, A., and Sterling, J. D., 2006, "Electrowetting Droplet Microfluidics on a Single Planar Surface," Microfluid. Nanofluid., **2**(5), pp. 435–446.

[4] Lannutti, J., Reneker, D., Ma, T., Tomasko, D., and Farson, D., 2007, "Electrospinning for Tissue Engineering Scaffolds," Mater. Sci. Eng., C, **27**(3), pp. 504–509.

[5] Wang, S., Zhu, J., Shao, Y., Li, W., Wu, Y., Zhang, L., and Hao, X., 2017, "Three-Dimensional MoS2@ CNT/RGO Network Composites for High-Performance Flexible Supercapacitors," Chem. – Eur. J., **23**(14), pp. 3438–3446.

[6] Lin, Y., Zhou, R., and Xu, J., 2018, "Superhydrophobic Surfaces Based on Fractal and Hierarchical Microstructures Using Two-Photon Polymerization: Toward Flexible Superhydrophobic Films," Adv. Mater. Interfaces, **5**(21), p. 1801126.

[7] Thangaraju, E., and Dhanapal, D., 2020, "Biocompatible Electrospun Nanofibrous Scaffold for Oral Cancer Treatment," *Biological Synthesis of Nanoparticles and Their Applications*, CRC Press, Boca Raton, FL, p. 221.

[8] Stanton, M. M., Trichet-Paredes, C., and Sánchez, S., 2015, "Applications of Three-Dimensional (3D) Printing for Microswimmers and Bio-Hybrid Robotics," Lab Chip, **15**(7), pp. 1634–1637.

[9] Ensikat, H. J., Ditsche-Kuru, P., Neinhuis, C., and Barthlott, W., 2011, "Superhydrophobicity in Perfection: The Outstanding Properties of the Lotus Leaf," Beilstein J. Nanotechnol., **2**(1), pp. 152–161.

[10] Barthlott, W., and Neinhuis, C., 1997, "Purity of the Sacred Lotus, or Escape From Contamination in Biological Surfaces," Planta, **202**(1), pp. 1–8.

[11] Barthlott, W., Mail, M., and Neinhuis, C., 2016, "Superhydrophobic Hierarchically Structured Surfaces in Biology: Evolution, Structural Principles and Biomimetic Applications," Philos. Trans. R. Soc., A, **374**(2073), p. 20160191.

[12] Koch, K., and Barthlott, W., 2009, "Superhydrophobic and Superhydrophilic Plant Surfaces: An Inspiration for Biomimetic Materials," Philos. Trans. R. Soc., A, **367**(1893), pp. 1487–1509.

[13] Jagels, R., 1994, "Leaf Wettability as a Measure of Air Pollution Effects,"*Air Pollutants and the Leaf Cuticle*, Springer, Heidelberg, pp. 97–105.

[14] Xie, G., Zhang, G., Lin, F., Zhang, J., Liu, Z., and Mu, S., 2008, "The Fabrication of Subwavelength Anti-Reflective Nanostructures Using a Bio-Template," Nanotechnology, **19**(9), p. 095605.

[15] Schulte, A. J., Droste, D. M., Koch, K., and Barthlott, W., 2011, "Hierarchically Structured Superhydrophobic Flowers With Low Hysteresis of the Wild Pansy (*Viola tricolor*)–New Design Principles for Biomimetic Materials," Beilstein J. Nanotechnol., **2**(1), pp. 228–236.

[16] Schulte, A. J., Mail, M., Hahn, L. A., and Barthlott, W., 2019, "Ultraviolet Patterns of Flowers Revealed in Polymer Replica–Caused by Surface Architecture," Beilstein J. Nanotechnol., **10**(1), pp. 459–466.

[17] Guo, H.-Y., Li, Q., Zhao, H.-P., Zhou, K., and Feng, X.-Q., 2015, "Functional Map of Biological and Biomimetic Materials With Hierarchical Surface Structures," RSC Adv., **5**(82), pp. 66901–66926.

[18] Barthlott, W., Mail, M., Bhushan, B., and Koch, K., 2017, "Plant Surfaces: Structures and Functions for Biomimetic Innovations," Nano-Micro Lett., **9**(2), p. 23.

[19] Linklater, D. P., Duy Nguyen, H. K., Bhadra, C. M., Juodkazis, S., and Ivanova, E. P., 2017, "Influence of Nanoscale Topology on Bactericidal Efficiency of Black Silicon Surfaces," Nanotechnology, **28**(24), p. 245301.

[20] Bandara, C. D., Singh, S., Afara, I. O., Wolff, A., Tesfamichael, T., Ostrikov, K., and Oloyede, A., 2017, "Bactericidal Effects of Natural Nanotopography of

Dragonfly Wing on *Escherichia coli*," ACS Appl. Mater. Interfaces, **9**(8), pp. 6746–6760.
[21] Liu, Y., Yin, X., Zhang, J., Wang, Y., Han, Z., and Ren, L., 2013, "Biomimetic Hydrophobic Surface Fabricated by Chemical Etching Method From Hierarchically Structured Magnesium Alloy Substrate," Appl. Surf. Sci., **280**, pp. 845–849.
[22] Xu, W., Liu, H., Lu, S., Xi, J., and Wang, Y., 2008, "Fabrication of Superhydrophobic Surfaces With Hierarchical Structure Through a Solution-Immersion Process on Copper and Galvanized Iron Substrates," Langmuir, **24**(19), pp. 10895–10900.
[23] Cao, W., Jiang, L., Hu, J., Wang, A., Li, X., and Lu, Y., 2018, "Optical Field Enhancement in Au Nanoparticle-Decorated Nanorod Arrays Prepared by Femtosecond Laser and Their Tunable Surface-Enhanced Raman Scattering Applications," ACS Appl. Mater. Interfaces, **10**(1), pp. 1297–1305.
[24] Zhang, G., Zhang, J., Xie, G., Liu, Z., and Shao, H., 2006, "Cicada Wings: A Stamp From Nature for Nanoimprint Lithography," Small, **2**(12), pp. 1440–1443.
[25] Yao, X., Chen, Q., Xu, L., Li, Q., Song, Y., Gao, X., Quéré, D., and Jiang, L., 2010, "Bioinspired Ribbed Nanoneedles With Robust Superhydrophobicity," Adv. Funct. Mater., **20**(4), pp. 656–662.
[26] Shang, B., Wang, Y., Peng, B., and Deng, Z., 2016, "Bioinspired Polydopamine Particles-Assisted Construction of Superhydrophobic Surfaces for Oil/Water Separation," J. Colloid Interface Sci., **482**, pp. 240–251.
[27] Chen, F., Zhang, D., Yang, Q., Yong, J., Du, G., Si, J., Yun, F., and Hou, X., 2013, "Bioinspired Wetting Surface via Laser Microfabrication," ACS Appl. Mater. Interfaces, **5**(15), pp. 6777–6792.
[28] Kuo, W.-K., Hsu, J.-J., Nien, C.-K., and Yu, H. H., 2016, "Moth-Eye-Inspired Biophotonic Surfaces With Antireflective and Hydrophobic Characteristics," ACS Appl. Mater. Interfaces, **8**(46), pp. 32021–32030.
[29] Ridaoui, H., Wieder, F., Ponche, A., and Soppera, O., 2010, "Direct ArF Laser Photopatterning of Metal Oxide Nanostructures Prepared by the Sol–Gel Route," Nanotechnology, **21**(6), p. 065303.
[30] Gonsalves, K. E., Wang, M., Lee, C.-T., Yueh, W., Tapia-Tapia, M., Batina, N., and Henderson, C. L., 2009, "Novel Chemically Amplified Resists Incorporating Anionic Photoacid Generator Functional Groups for Sub-50-nm Half-Pitch Lithography," J. Mater. Chem., **19**(18), pp. 2797–2802.
[31] Campbell, M. T. H. R. G. D. M., Sharp, D. N., Harrison, M. T., Denning, R. G., and Turberfield, A. J., 2000, "Fabrication of Photonic Crystals for the Visible Spectrum by Holographic Lithography," Nature, **404**(6773), pp. 53–56.
[32] Lewis, J. A., and Gratson, G. M., 2004, "Direct Writing in Three Dimensions," Mater. Today, **7**(7–8), pp. 32–39.
[33] Joyee, E. B., Szmelter, A., Eddington, D. T., and Pan, Y., "Magnetic-Field-Assisted Stereolithography for Productions of Multi-Material Hierarchical Surface Structures," ACS Appl. Mater. Interfaces, **12**(37), pp. 42357–42368.
[34] Wu, D., Fang, N., Sun, C., and Zhang, X., 2006, "Stiction Problems in Releasing of 3D Microstructures and Its Solution," Sens. Actuators, A, **128**(1), pp. 109–115.
[35] Shevchenko, E. V., Talapin, D. V., Rogach, A. L., Kornowski, A., Haase, M., and Weller, H., 2002, "Colloidal Synthesis and Self-Assembly of CoPt3 Nanocrystals," J. Am. Chem. Soc., **124**(38), pp. 11480–11485.
[36] Heuberger, A., 1986, "X-ray Lithography," Microelectron. Eng., **5**(1–4), pp. 3–38.
[37] Ushiba, S., Shoji, S., Masui, K., Kuray, P., Kono, J., and Kawata, S., 2013, "3D Microfabrication of Single-Wall Carbon Nanotube/Polymer Composites by Two-Photon Polymerization Lithography," Carbon, **59**, pp. 283–288.
[38] Xing, J.-F., Zheng, M.-L., and Duan, X.-M., 2015, "Two-Photon Polymerization Microfabrication of Hydrogels: An Advanced 3D Printing Technology for Tissue Engineering and Drug Delivery," Chem. Soc. Rev., **44**(15), pp. 5031–5039.
[39] Spangenberg, A., Hobeika, N., Stehlin, F., Malval, J.-P., Wieder, F., Prabhakaran, P., Baldeck, P., and Soppera, O., 2013, "Recent Advances in Two-Photon Stereolithography," Updates in Advanced Lithography, IntechOpen, Knightsbridge, pp. 35–63.
[40] Gou, X., Zheng, M., Zhao, Y., Dong, X., Jin, F., Xing, J., and Duan, X., 2017, "Mechanical Property of PEG Hydrogel and the 3D Red Blood Cell Microstructures Fabricated by Two-Photon Polymerization," Appl. Surf. Sci., **416**, pp. 273–280.
[41] Xing, J., Liu, L., Song, X., Zhao, Y., Zhang, L., Dong, X., Jin, F., Zheng, M., and Duan, X., 2015, "3D Hydrogels With High Resolution Fabricated by Two-Photon Polymerization With Sensitive Water Soluble Initiators," J. Mater. Chem. B, **3**(43), pp. 8486–8491.
[42] Zyla, G., Kovalev, A., Grafen, M., Gurevich, E. L., Esen, C., Ostendorf, A., and Gorb, S., 2017, "Generation of Bioinspired Structural Colors via Two-Photon Polymerization," Sci. Rep., **7**(1), pp. 1–9.
[43] Ha, C. W., Prabhakaran, P., Son, Y., Lee, K.-S., and Yang, D.-Y., 2017, "Effective Direct Writing of Hierarchical 3D Polymer Micromeshes by Continuous Out-of-Plane Longitudinal Scanning," Macromol. Res., **25**(11), pp. 1129–1134.
[44] Lee, K.-S., Kim, R. H., Yang, D.-Y., and Park, S. H., 2008, "Advances in 3D Nano/Microfabrication Using Two-Photon Initiated Polymerization," Prog. Polym. Sci., **33**(6), pp. 631–681.
[45] Thakur, A., Banerjee, A. G., and Gupta, S. K., 2009, "A Survey of CAD Model Simplification Techniques for Physics-Based Simulation Applications," Comput. Aided Des., **41**(2), pp. 65–80.
[46] Kelleher, S. M., Habimana, O., Lawler, J., O'reilly, B., Daniels, S., Casey, E., and Cowley, A., 2016, "Cicada Wing Surface Topography: An Investigation Into the Bactericidal Properties of Nanostructural Features," ACS Appl. Mater. Interfaces, **8**(24), pp. 14966–14974.
[47] Wenzel, R. N., 1936, "Resistance of Solid Surfaces to Wetting by Water," Ind. Eng. Chem., **28**(8), pp. 988–994.
[48] Kawata, S., Sun, H.-B., Tanaka, T., and Takada, K., 2001, "Finer Features for Functional Microdevices," Nature, **412**(6848), pp. 697–698.
[49] Sikder, S., Barari, A., and Kishawy, H. A., 2014, "Effect of Adaptive Slicing on Surface Integrity in Additive Manufacturing," International Design Engineering Technical Conferences and Computers and Information in Engineering Conference, Buffalo, NY, Aug. 17–20, American Society of Mechanical Engineers, Vol. 46285, p. V01AT02A052.
[50] Barbieri, L., Wagner, E., and Hoffmann, P., 2007, "Water Wetting Transition Parameters of Perfluorinated Substrates With Periodically Distributed Flat-Top Microscale Obstacles," Langmuir, **23**(4), pp. 1723–1734.
[51] Wei, L., Parhi, P., Vogler, E. A., Ritty, T. M., and Lakhtakia, A., 2010, "Thickness-Controlled Hydrophobicity of Fibrous Parylene-C Films," Mater. Lett., **64**(9), pp. 1063–1065.
[52] Phillips, B. M., Jiang, P., and Jiang, B., 2011, "Biomimetic Broadband Antireflection Gratings on Solar-Grade Multicrystalline Silicon Wafers," Appl. Phys. Lett., **99**(19), p. 191103.
[53] Ahn, H.-J., Kim, S.-I., Yoon, J.-C., Lee, J.-S., and Jang, J.-H., 2012, "Power Conversion Efficiency Enhancement Based on the Bio-Inspired Hierarchical Antireflection Layer in Dye Sensitized Solar Cells," Nanoscale, **4**(15), pp. 4464–4469.
[54] Wang, H., Zhao, J., Zhu, Y., Meng, Y., and Zhu, Y., 2013, "The Fabrication, Nano/Micro-Structure, Heat-and Wear-Resistance of the Superhydrophobic PPS/PTFE Composite Coatings," J. Colloid Interface Sci., **402**, pp. 253–258.
[55] Cieślik, M., Zimowski, S., Gołda, M., Engvall, K., Pan, J., Rakowski, W., and Kotarba, A., 2012, "Engineering of Bone Fixation Metal Implants Biointerface—Application of Parylene C as Versatile Protective Coating," Mater. Sci. Eng., C, **32**(8), pp. 2431–2435.
[56] Xiong, W., Liu, Y., Jiang, L. J., Zhou, Y. S., Li, D. W., Jiang, L., Silvain, J., and Lu, Y. F., 2016, "Laser-Directed Assembly of Aligned Carbon Nanotubes in Three Dimensions for Multifunctional Device Fabrication," Adv. Mater., **28**(10), pp. 2002–2009.
[57] Sakellari, I., Gaidukeviciute, A., Giakoumaki, A., Gray, D., Fotakis, C., Farsari, M., Vamvakaki, M., Reinhardt, C., Ovsianikov, A., and Chichkov, B. N., 2010, "Two-Photon Polymerization of Titanium-Containing Sol–Gel Composites for Three-Dimensional Structure Fabrication," Appl. Phys. A, **100**(2), pp. 359–364.
[58] Suter, M., Zhang, L., Siringil, E. C., Peters, C., Luehmann, T., Ergeneman, O., Peyer, K. E., Nelson, B. J., and Hierold, C., 2013, "Superparamagnetic Microrobots: Fabrication by Two-Photon Polymerization and Biocompatibility," Biomed. Microdevices, **15**(6), pp. 997–1003.